Supporting Information

Boosting the Electro-oxidation of 5-Hydroxymethyl-furfural on Co-CoS_x Heterojunction by Intensified Spin Polarization

Jianmin Chen, Yajing Wang*, Mingjun Zhou, and Yingwei Li*

State Key Laboratory of Pulp and Paper Engineering, School of Chemistry and Chemical Engineering, South China University of Technology, Guangzhou 510640, China.

*Corresponding authors

E-mail: wangyj4302@scut.edu.cn; liyw@scut.edu.cn

Experimental section

Chemicals

All chemicals were purchased from commercial sources and used without further treatments.

Materials preparation

Preparation of ZIF-67

4 mmol of $Co(NO_3)_2 \cdot 6H_2O$ and 16 mmol of 2-methylimidazole (2-MIM) were dissolved into 200 mL of methanol with ultrasonic treatment for 1 min, respectively. Then, the 2-MIM solution was poured into the $Co(NO_3)_2 \cdot 6H_2O$ solution and vigorously stirred for 24 h. The resultant ZIF-67 was collected and washed with methanol for three times. Finally, the product was dried at 60 ℃overnight.

Preparation of Co@NC with different structures

ZIF-67 was pyrolyzed at 500 °C for 3 h with a heating rate of 2 ℃ min^{-1} under flowing H_2/Ar (V_{H2}:V_{Ar} = 1:9) atmosphere to obtain Co@CN. Subsequently, the Co@CN was treated at 200, 300, 400, and 500 ℃ under Ar atmosphere for 3 h to obtain yolk-shelled Y-Co@CN-T (T = 200, 300, 400, and 500 ℃). For comparison, hollow Co@CN was prepared through pyrolyzing ZIF-67 at 700 ℃ for 3 h under H_2/Ar atmosphere. In addition, the double-shelled D-Co@CN could be obtained by pyrolyzing Co@CN at 300 ℃ for 8 h under Ar atmosphere.

Preparation of Co-CoS_x@NC with different structures

100 mg of Y-Co@CN was placed in tubular furnace, with thiourea in a upstream. Then, the sample was heated at 300 ℃ for 2 h with a heating rate of 2 ℃ min^{-1} under Ar atmosphere to obtain Y-Co-$CoS_{1.097}$@CN, Y-Co-CoS_x@CN, Y-Co-CoS_2@CN, and Y-CoS_2@CN by controlling the amount of thiourea. For comparison, the synthesis procedures of Co-CoS_x@NC, H-Co-CoS_x@NC, and D-Co-CoS_x@NC were similar to that of Y-Co-CoS_x@CN.

Preparation of Co-CoP@NC with different structures

The synthesis procedures of Co-CoP@CN, H-Co-CoP@CN, Y-Co-CoP@CN, and D-Co-CoP@CN were similar to those of Co-CoS_x@NC, H-Co-CoS_x@NC, Y-Co-CoS_x@NC, and D-Co-CoS_x@NC, respectively, except for using NaH_2PO_2 as P source.

Characterization

X-ray diffraction (XRD) measurements were performed using a Bruker D8 ADVANCE equipped with Cu Kα radiation (λ = 0.1543 nm). High-resolution transmission electron microscope (HRTEM) and high angle annular dark-field scanning transmission electron microscopy (HAADF-STEM) images were acquired on JEOL JEM-2100F with EDX analysis (Bruker Xflash 5030T), operated at 200 kV. Specific surface areas and pore structures were measured by N_2 adsorption/desorption at 77 K on a Micromeritics ASAP 2020 M instrument. X-ray photoelectron spectroscopy (XPS) measurements were carried out on Thermo Scientific K-Alpha. Raman spectra were collected on a LabRAM Aramis Raman Spectrometer (HORIBA Jobin Yvon). The cobalt contents in the samples were measured quantitatively by

Atomic Absorption Spectroscopy (AAS, HITACHI Z-2300 instrument). The contents of C and N were analyzed by an Elementar Vario EL III equipment. X-ray absorption fine structure (XAFS) technique was used to investigate the electronic properties and local chemical environment of Co species on samples. XAFS experiments were implemented at the 1W1B station of Beijing Synchrotron Radiation Facility.

Electrochemical measurements

All the electrochemical measurements were conducted in a conventional three-electrode cell by using CHI 760E potentiostat (CH Instruments) at room temperature, in which the platinum net and Ag/AgCl (saturated KCl) were used as the counter and reference electrodes, respectively. 1.0 mg of electrocatalyst was uniformly dispersed into a mixed solution of 20 μL Nafion and 300 μL ethanol, and then which was coated on a piece of clean carbon cloth (1×1 cm) as a working electrode. All the measured potentials *vs.* the Ag/AgCl reference electrode were converted to the reversible hydrogen electrode (RHE) scale through the Nernst equation: $E_{[RHE]} = E_{[Ag/AgCl]} + 0.197 + 0.059$ pH.

The electrochemical HMF oxidation tests were conducted in 0.1 M KOH (20 mL) solution with 5 mM HMF. All electrochemical reaction was carried out at room temperature (25 ± 1 °C). The Linear-sweep voltammetry (LSV) measurements were performed at a scan rate of 5 mV s^{-1} with 80% iR compensation in all the electrochemical tests. The CVs with different scan rates (10, 20, 30, 40, 50, 60, 70, and 80 mV/s) between the potential intervals of 0.54 to 0.64 *vs.* RHE were tested to calculate the double-layer capacitance (C_{dl}). The conversions of electrochemical HMF

oxidation were evaluated by chronoamperometry at 1.40 V_{RHE}, while the electrolyte was stirred with a magnetic stir bar. The electrolyte was stirred with a magnetic stir bar at a constant potential (1.40 V *vs.* RHE) until passing 58 C of charges (the stoichiometric number of Coulombs to convert the given amount of HMF to FDCA is 57.8 C). For reusability tests, the work electrode compartment was washed with KOH (0.1 M), and used for the next test. Especially, 5 mg of electrocatalyst was uniformly dispersed on a piece of clean carbon cloth (10×10 cm) as a working electrode for the potentiostatic electrolysis of 50 mM HMF. Electrochemical impedance spectroscopy (EIS) measurements were performed in the frequency ranging from 0.01 to 10^5 Hz with amplitude of 10 mV.

Products analysis

High-performance liquid chromatography (HPLC, Shimadzu Prominence LC-2030C system) with a refractive index detector was used to analyze the HMF oxidation products. Sulfuric acid (5 mM) was used as the mobile phase in isocratic mode with a flow rate of 1 mL min^{-1} at 40 ℃. Sample aliquots (10 μL) were injected directly into a Shodex SUGARSH-1011 column (8 mm × 300 mm). The identification and quantification of products were obtained from the calibration curves by applying standard solutions with known concentrations. The retention times were 11.4, 14.8, 15.4, 21.5, and 26.2 min for FDCA, HMFCA, FFCA, HMF and DFF, respectively.

HMF conversion, FDCA yield and Faradaic efficiency were calculated according to the following equations:

$$\text{HMF conversion (\%)} = \frac{mol\ of\ HMF\ consumed}{mol\ of\ HMF\ added} \times 100 \quad (1)$$

$$\text{FDCA yield (\%)} = \frac{mol\ of\ FDCA\ formed}{mol\ of\ HMF\ added} \times 100 \quad (2)$$

$$\text{Faradaic efficiency (\%)} = \frac{mol\ of\ FDCA\ formed}{Charge\ /\ (6 \times F)} \times 100 \quad (3)$$

Where F (96485 C mol^{-1}) is the Faradaic constant.

Computational details

Density functional theory (DFT) calculations were performed using the quantum espresso (QE)[1, 2] based on the pseudopotential plane wave (PPW) method. The Perdew-Bueke-Ernzerhof (PBE) functional[3] was used to describe exchange-correlation effects of electrons. We have chosen the projected augmented wave (PAW) potentials[4, 5] to describe the ionic cores and take valence electrons into account using a plane wave basis set with a kinetic energy cutoff of 550 eV. In order to simulate the reaction procedure of HMF on substrate, three different slab models were built. (111) and (200) planes were selected to model the reaction on Co and CoS_2, respectively. In addition, a heterojunction structure was built by Co and CoS_2. During the geometry optimizations, all the atom positions were allowed to relax. In this work, the Brillouin-zone sampling were conducted using Monkhorst-Pack (MP)[6] grids of special points with the separation of 0.04 $Å^{-1}$. The convergence criterion for the electronic self-consistent field (SCF) loop was set to 1×10^{-5} eV/atom. The atomic structures were optimized until the residual forces were below 0.02 $eVÅ^{-1}$. To investigate the electron difference upon HMF absorption, differential charge density was calculated by $\Delta\rho = \rho_{total} - \rho_{sub} - \rho_{abs}$, where ρ_{total}, ρ_{sub}, and ρ_{abs} represent the

total charge density with HMF absorbed, charge density of substrate, and charge density of absorbed molecules. Besides standard DFT calculation, COHP calculations were also carried out by Lobster[7] to investigate the bonding strength between atoms

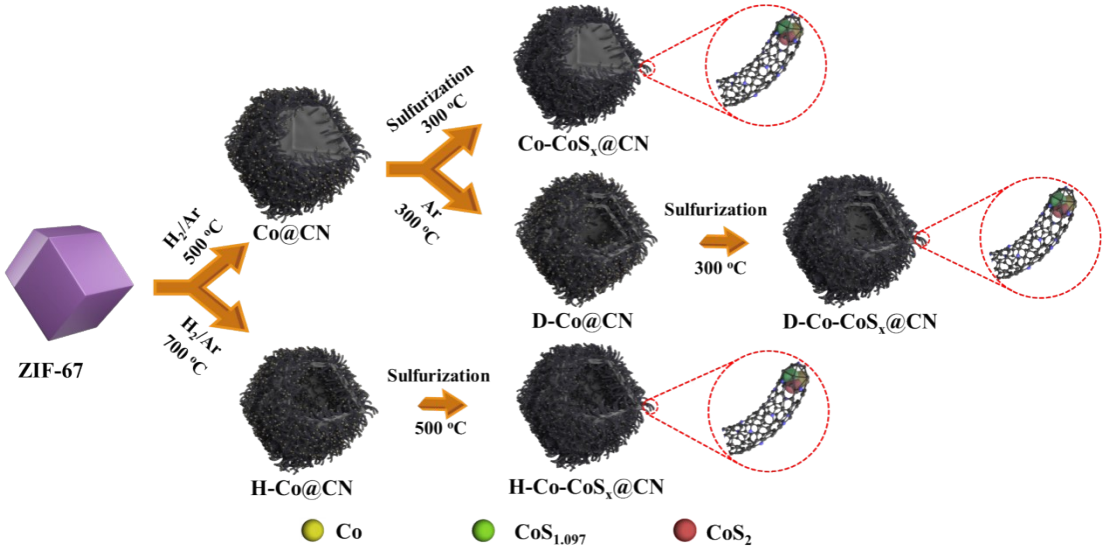

Scheme S1. Schematic illustration of the synthesis process for Co-CoS_x@CN, H-Co-CoS_x@CN, and D-Co-CoS_x@CN.

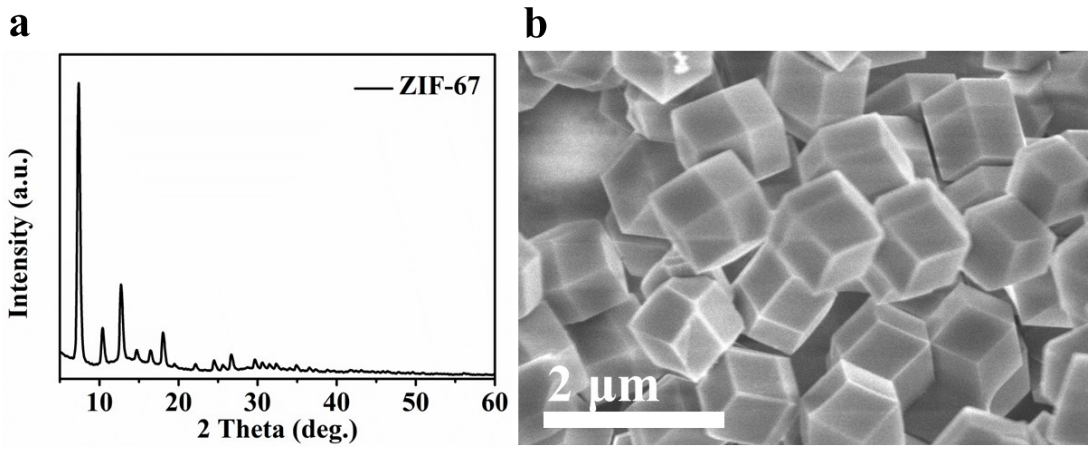

Figure S1. (a) XRD pattern and (b) SEM image of ZIF-67 crystals.

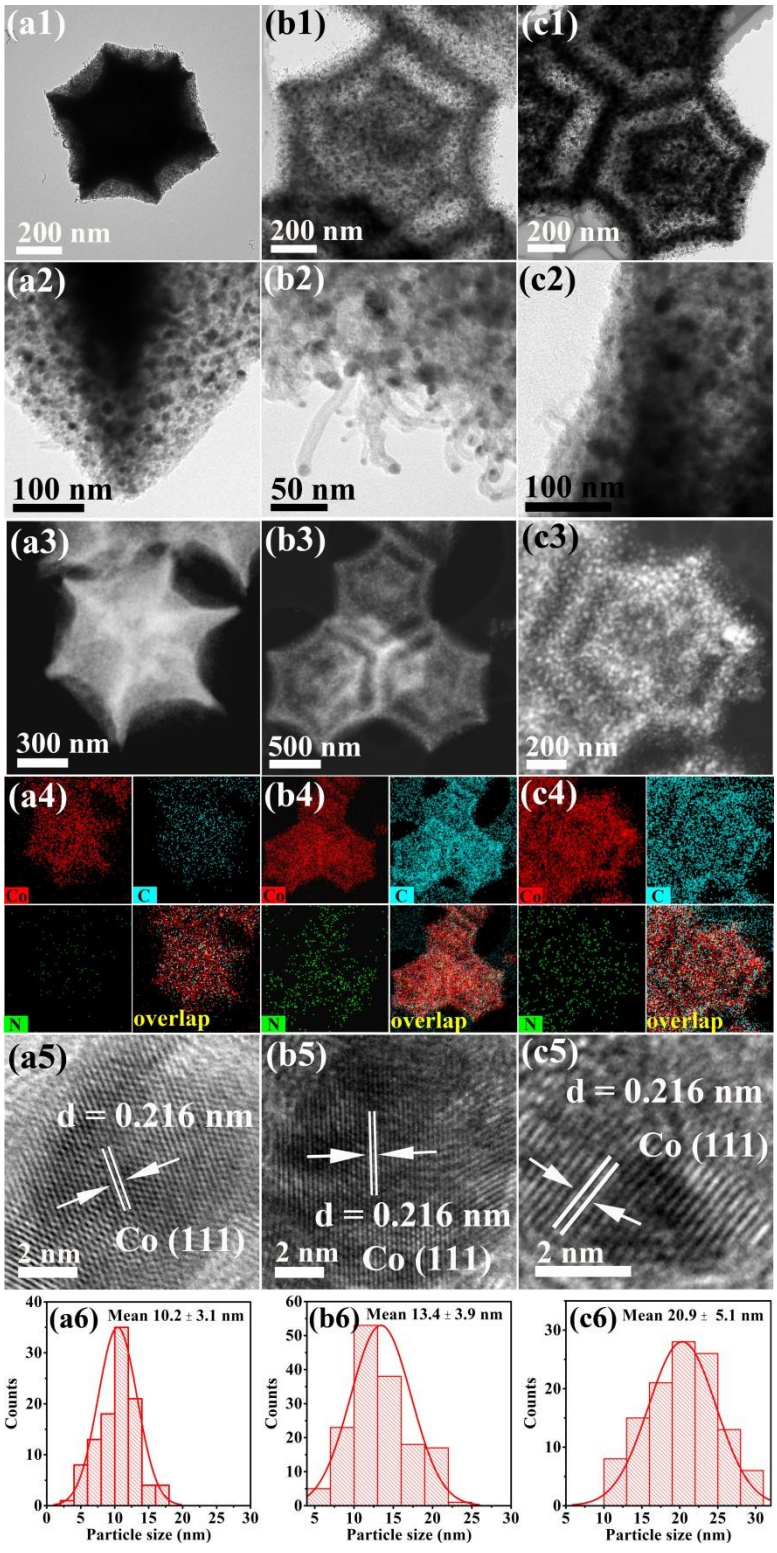

Figure S2. (a1-c1, a2-c2) TEM, (a3-c3) HAADF-STEM, (a4-c4) EDX mapping, (a5-c5) HRTEM images, and (a6-c6) Co particle size distributions of (a1-a6) Co@CN, (b1-b6) Y-Co@CN, and (c1-c6) D-Co@CN.

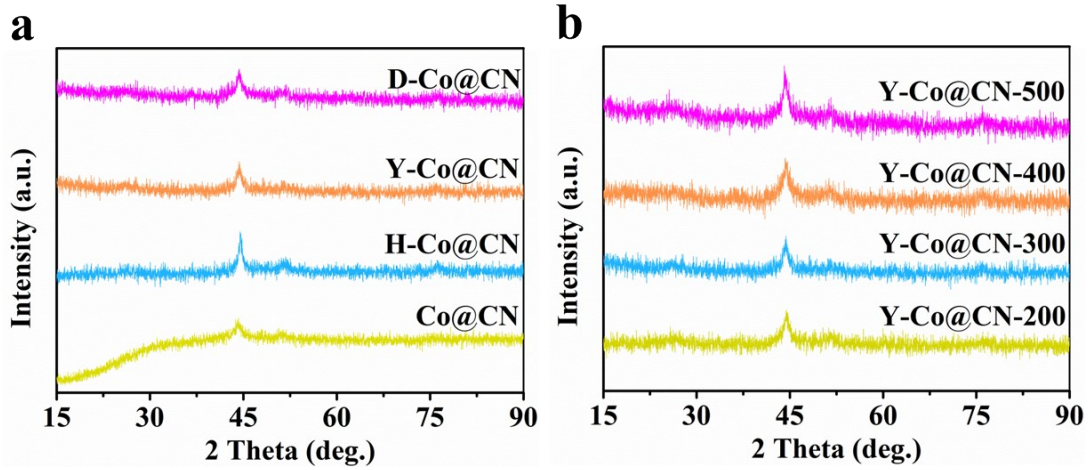

Figure S3. XRD patterns of different catalysts.

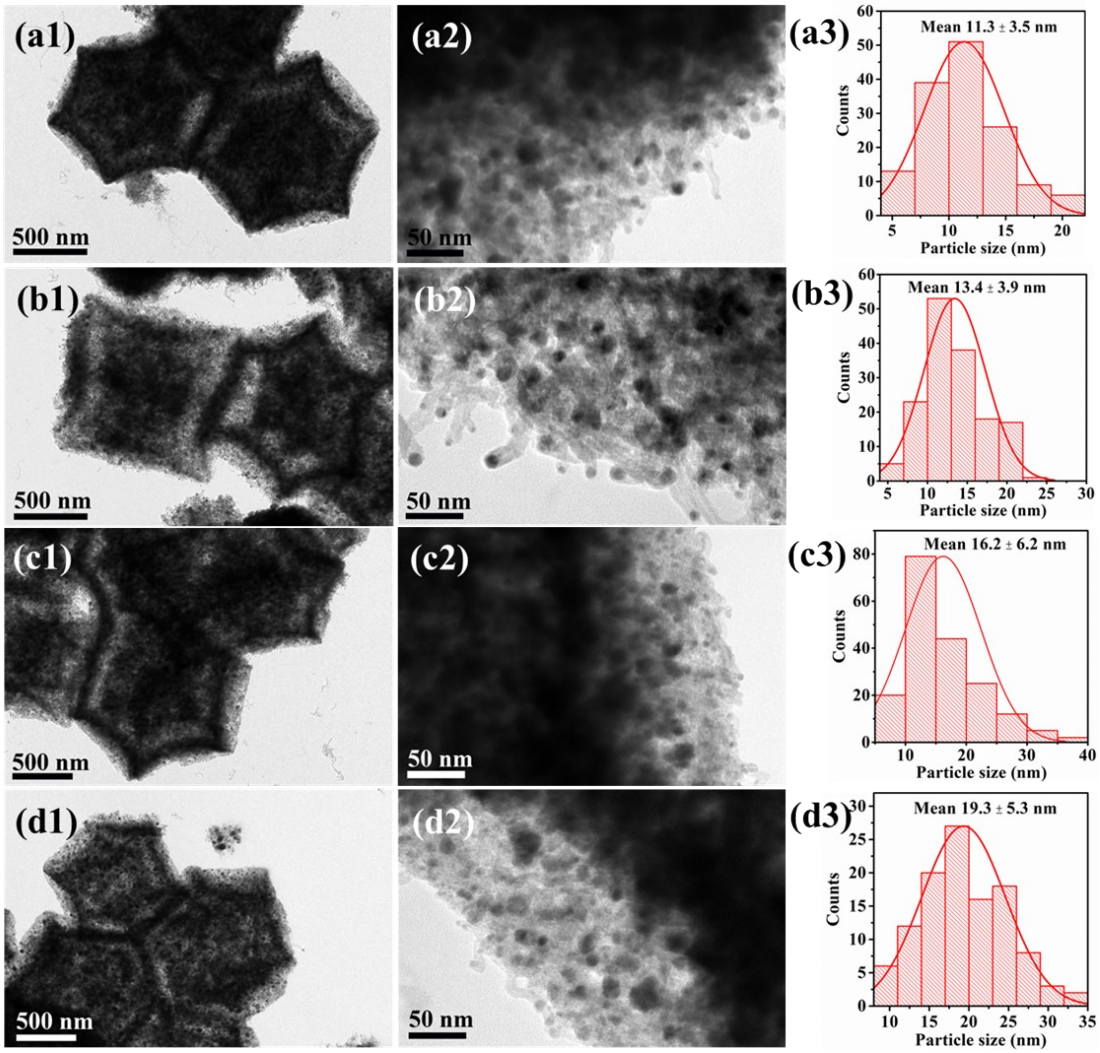

Figure S4. (a1-d1, a2-d2) TEM images and (a3, b3, c3, d3) Co particle size distributions of (a1-a3) Y-Co@CN-200, (b1-b3) Y-Co@CN-300, (c1-c3) Y-Co@CN-400, and (d1-d3) Y-Co@CN-500.

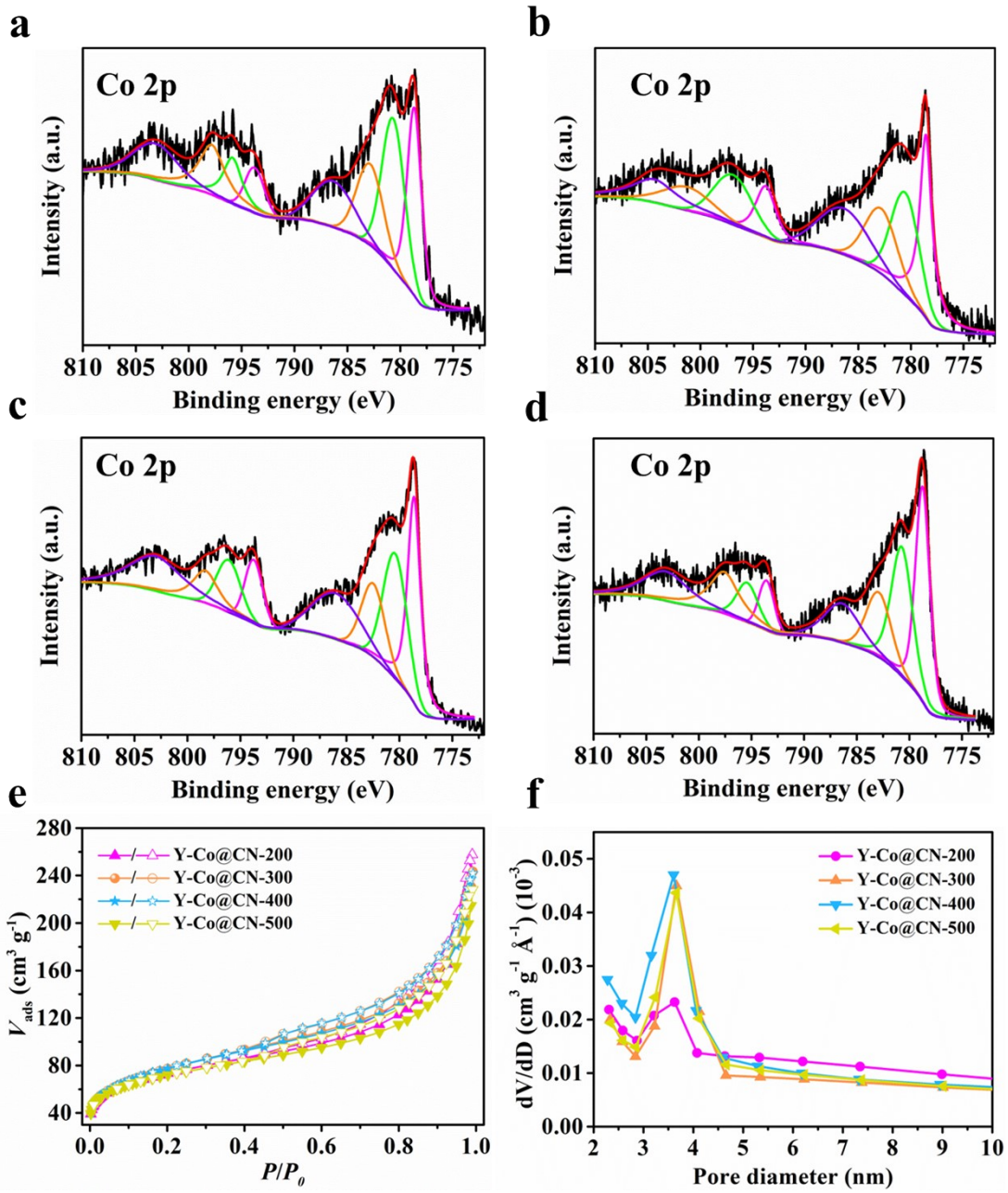

Figure S5. Co 2p XPS spectra of (a) Y-Co@CN-200, (b) Y-Co@CN-300, (c) Y-Co@CN-400, and (d) Y-Co@CN-500. (e) N_2 adsorption-desorption isotherms and, (f) pore size distributions of Y-Co@CN-200, Y-Co@CN-300, Y-Co@CN-400, and Y-Co@CN-500.

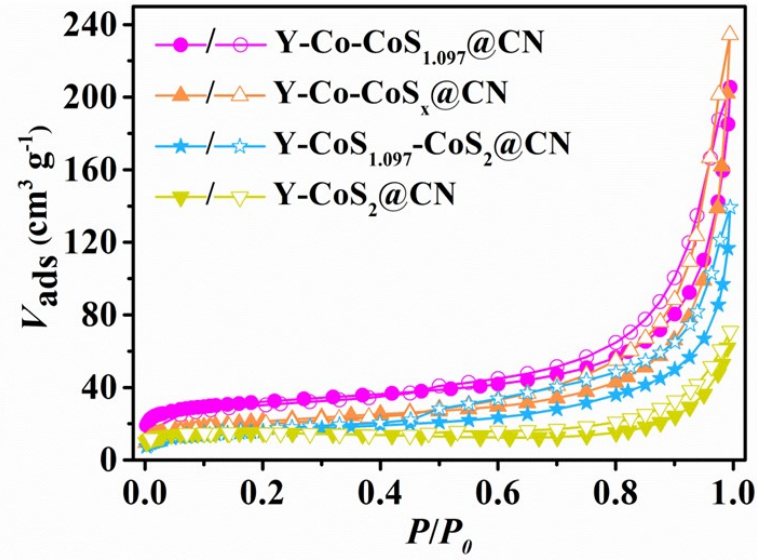

Figure S6. N_2 adsorption-desorption isotherms of different catalysts.

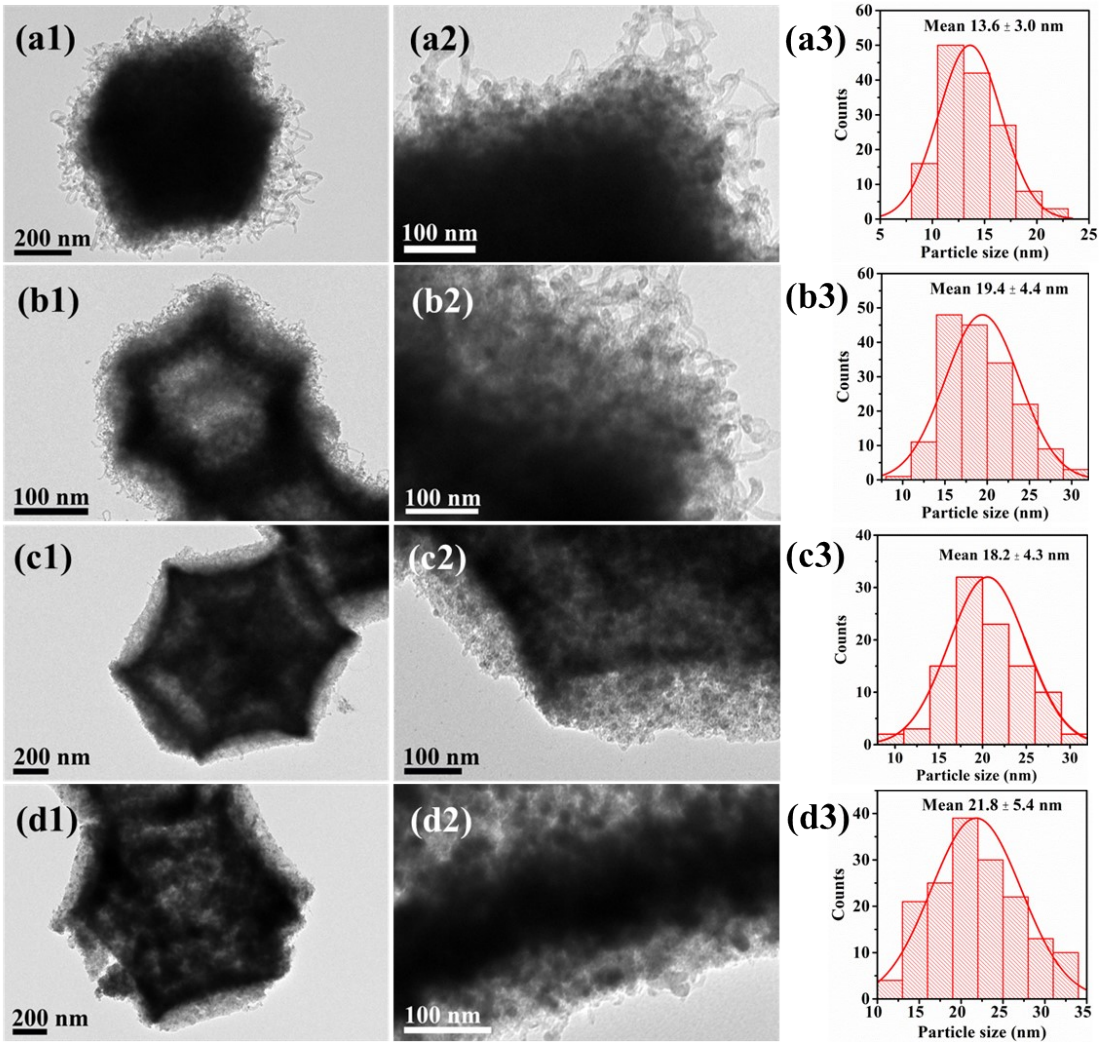

Figure S7. (a1-d1, a2-d2) TEM images and (a3-d3) the size distributions of Co-CoS_x NPs of (a1-a3) Co-CoS_x@CN, (b1-b3) H-Co-CoS_x@CN, (c1-c3) Y-Co-CoS_x@CN, and (d1-d3) D-Co-CoS_x@CN.

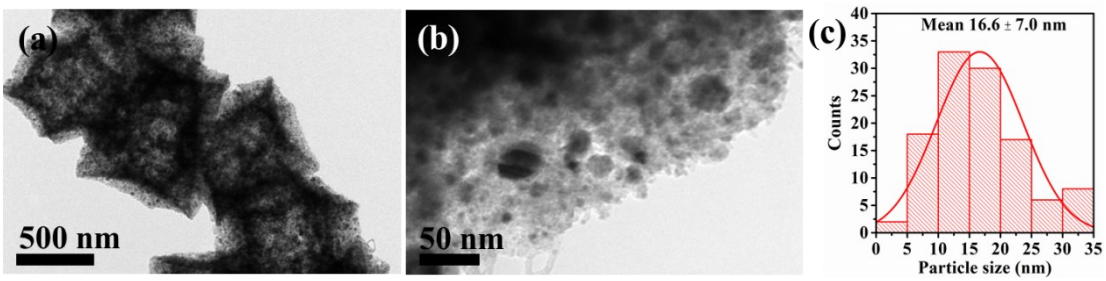

Figure S8. (a-b) TEM images and (c) Co particle size distribution of H-Co@CN.

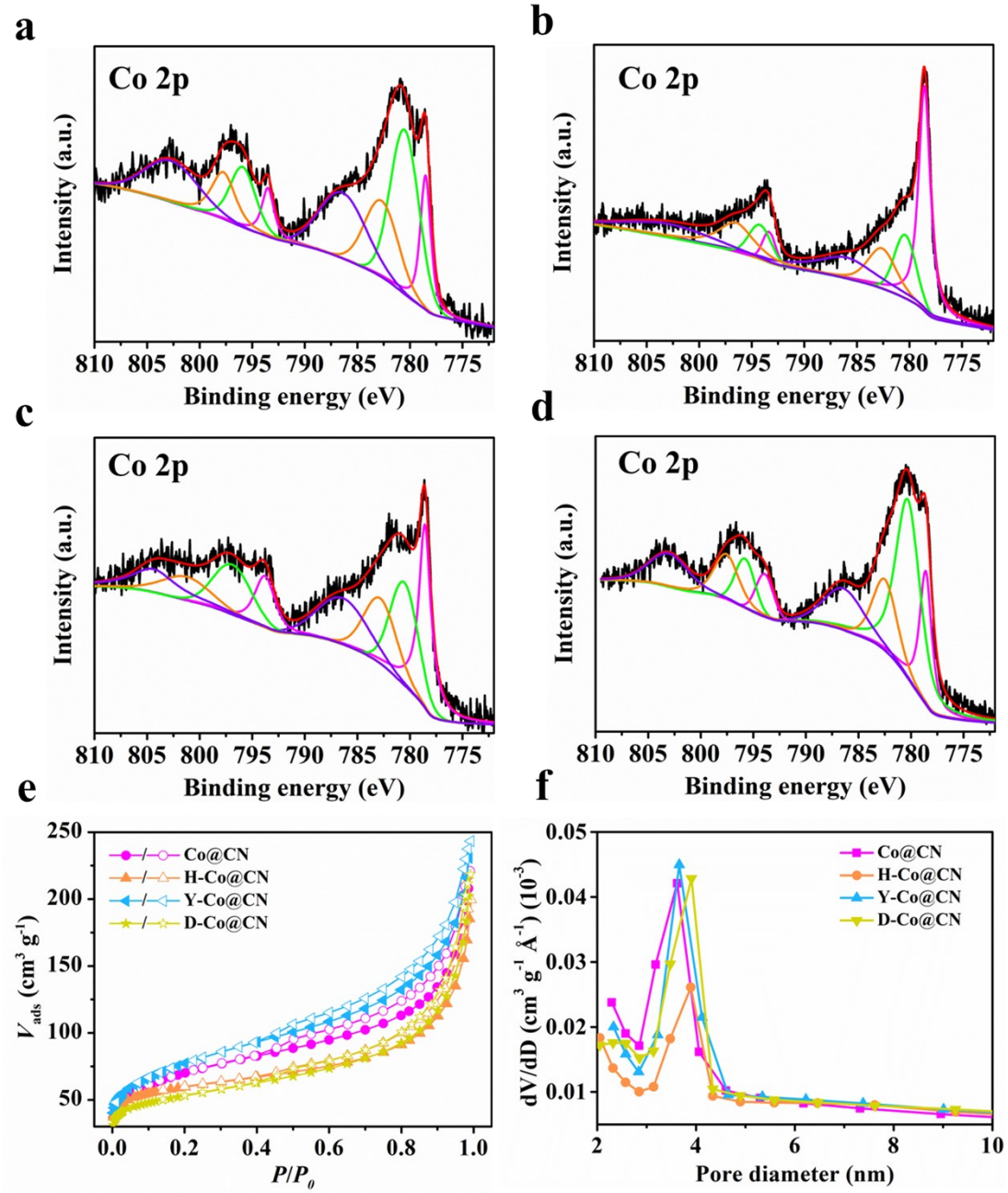

Figure S9. Co 2p XPS spectra of (a) Co@CN, (b) H-Co@CN, (c) Y-Co@CN, and (d) D-Co@CN. (e) N_2 adsorption-desorption isotherms, and (f) pore size distributions of Co@CN, H-Co@CN, Y-Co@CN, and D-Co@CN.

The specific surface areas of Co@CN, H-Co@CN, Y-Co@CN, and D-Co@CN are calculated to be 256, 200, 300, and 260 m^2/g, respectively.

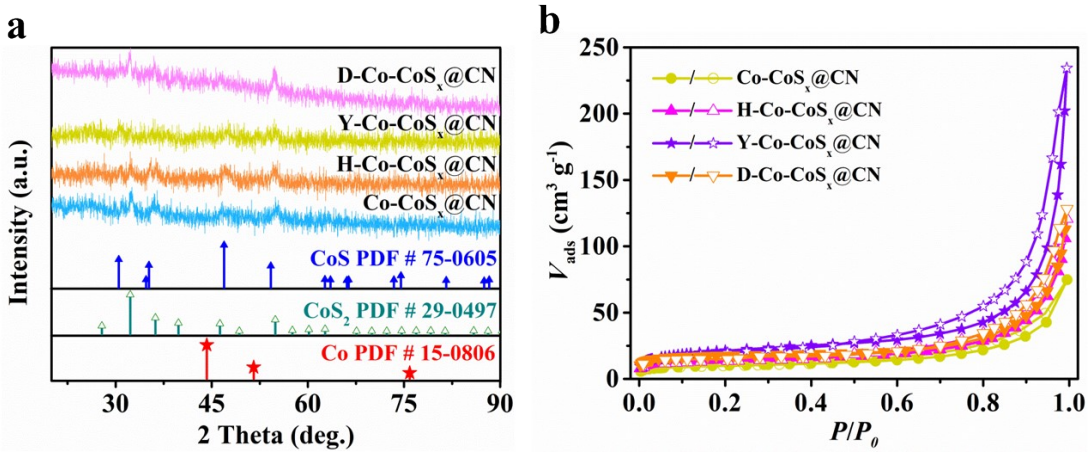

Figure S10. (a) XRD patterns and (b) N_2 adsorption-desorption isotherms of Co-CoS_x@CN, H-Co-CoS_x@CN, Y-Co-CoS_x@CN, and D-Co-CoS_x@CN.

The specific surface areas of Co-CoS_x@CN, H-Co-CoS_x@CN, Y-Co-CoS_x@CN, and D-Co-CoS_x@CN are calculated to be 33.3, 48.9, 74.0, 57.8 m^2/g (Figure S10b).

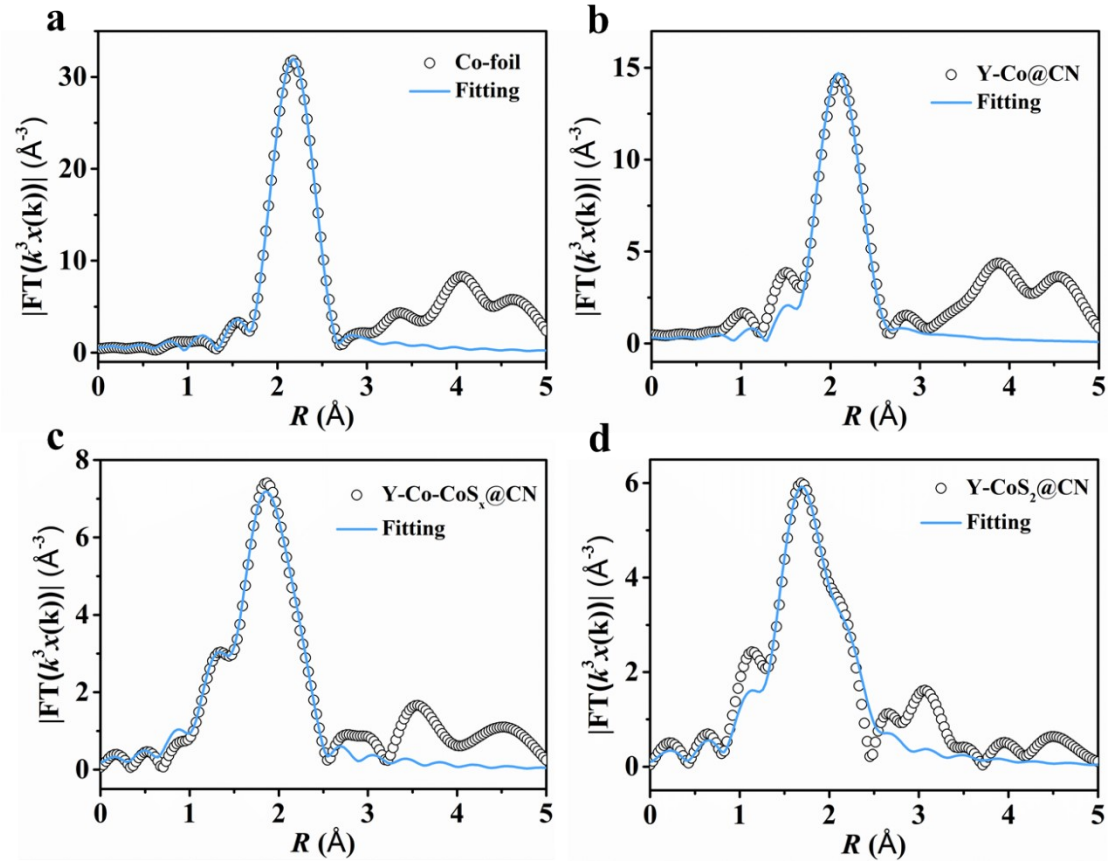

Figure S11. Co K-edge EXAFS fitting spectra of (a) Co foil, (b) Y-Co@CN, (c) Y-Co-CoS_x@CN, and (d) Y-Co-CoS_2@CN in R space.

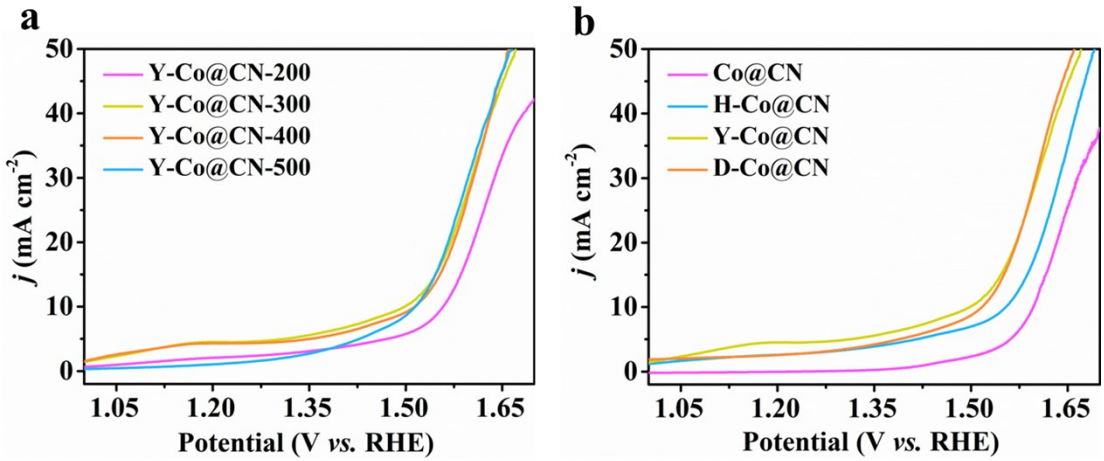

Figure S12. LSV curves of (a) Y-Co@CN-200, Y-Co@CN-300, Y-Co@CN-400, and Y-Co@CN-500 and (b) Co@CN, H-Co@CN, Y-Co@CN, D-Co@CN at a scan rate of 5 mV s^{-1} in 0.1 M KOH with 5 mM HMF.

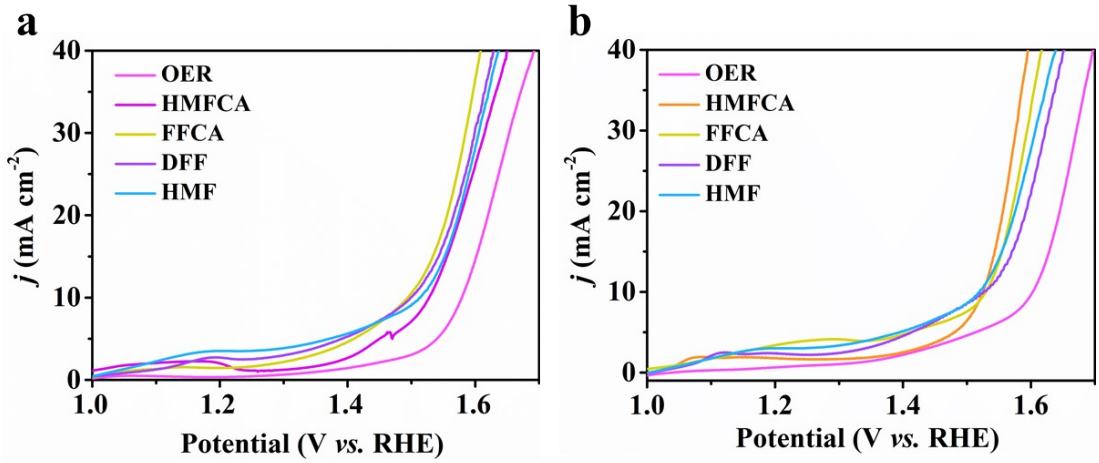

Figure S13. LSV curves of (a) Y-Co@CN and (b) Y-CoS_2@CN at a scan rate of 5 mV s^{-1} in 0.1 M KOH with the addition of 5 mM HMF, 5 mM DFF, 5 mM HMFCA, 5 mM FFCA, or without any organic substrate.

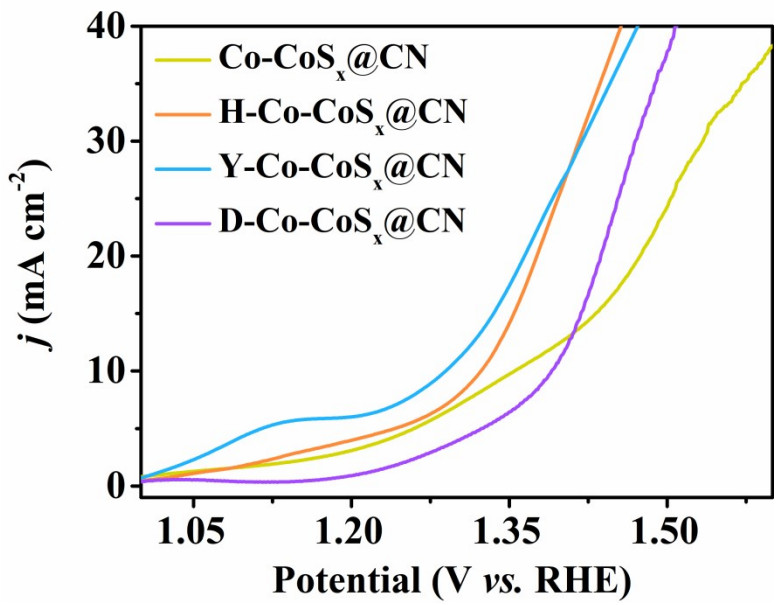

Figure S14. LSV curves of Co-CoS_x@CN, H-Co-CoS_x@CN, Y-Co-CoS_x@CN, and D-Co-CoS_x@CN at a scan rate of 5 mV s^{-1} in 0.1 M KOH with 5 mM HMF.

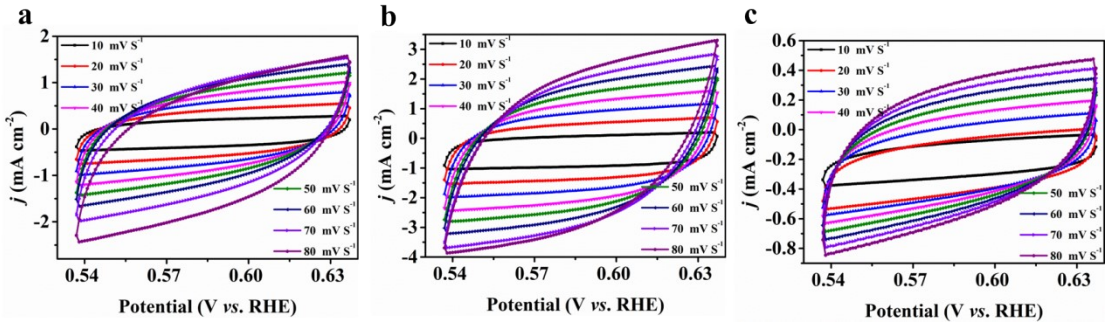

Figure S15. CV curves of Y-Co@CN, (b) Y-Co-CoS_x@CN, and (c) Y-CoS_2@CN with 5 mM HMF at different scan rates.

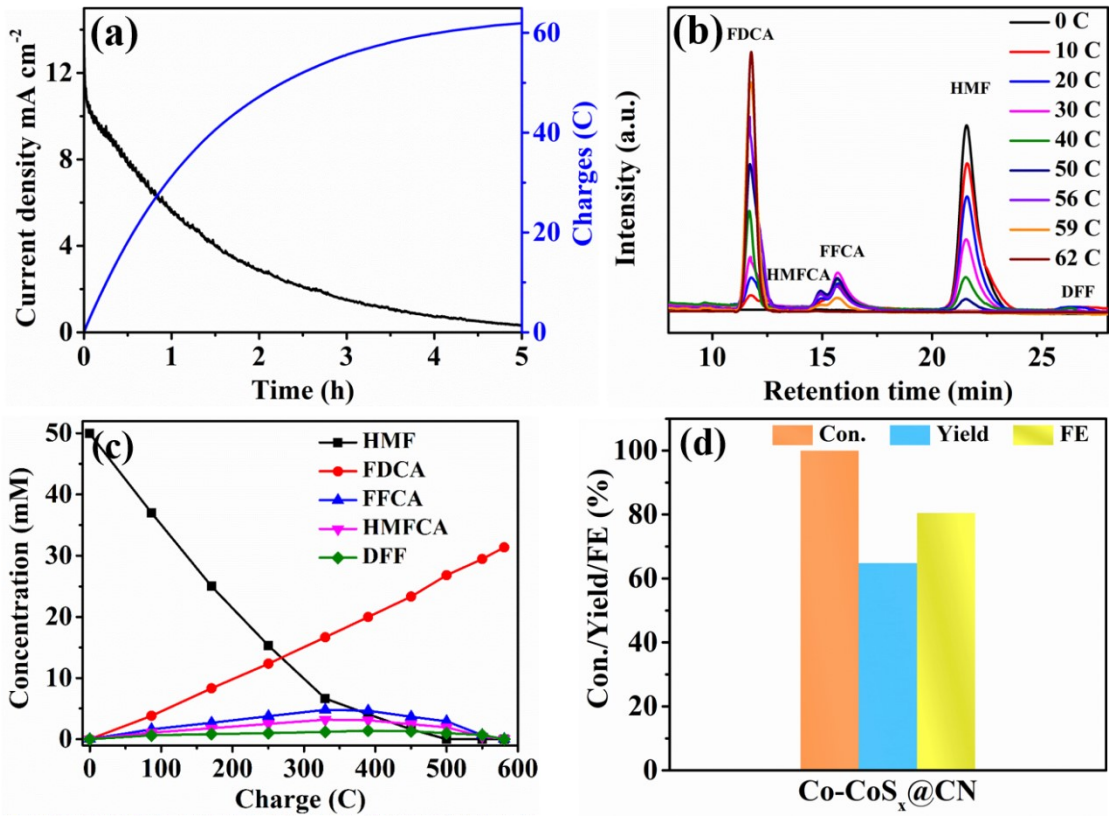

Figure S16. (a) I-t curve for Y-Co-CoS_x@CN at a constant potential of 1.40 V in 0.1 M KOH with 5 mM HMF, (b) HPLC traces of HMF electrooxidation catalyzed by Y-Co-CoS_x@CN at 1.40 V_{RHE} in 20 mL of 0.1 M KOH with 5 mM HMF. (c) The concentration of HMF and its oxidation products in 50 mM HMF electro-oxidation over Y-Co-CoS_x@CN. (d) HMF conversion, FDCA yield, and FE in 50 mM HMF electro-oxidation over Y-Co-CoS_x@CN.

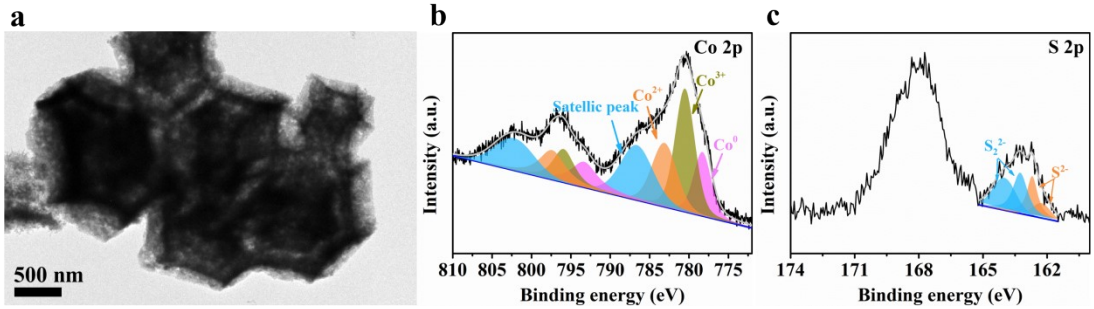

Figure S17. (a) TEM image, (b) Co 2p and (c) S 2p XPS spectra of Y-Co-CoS_x@CN after HMF electrooxidation test.

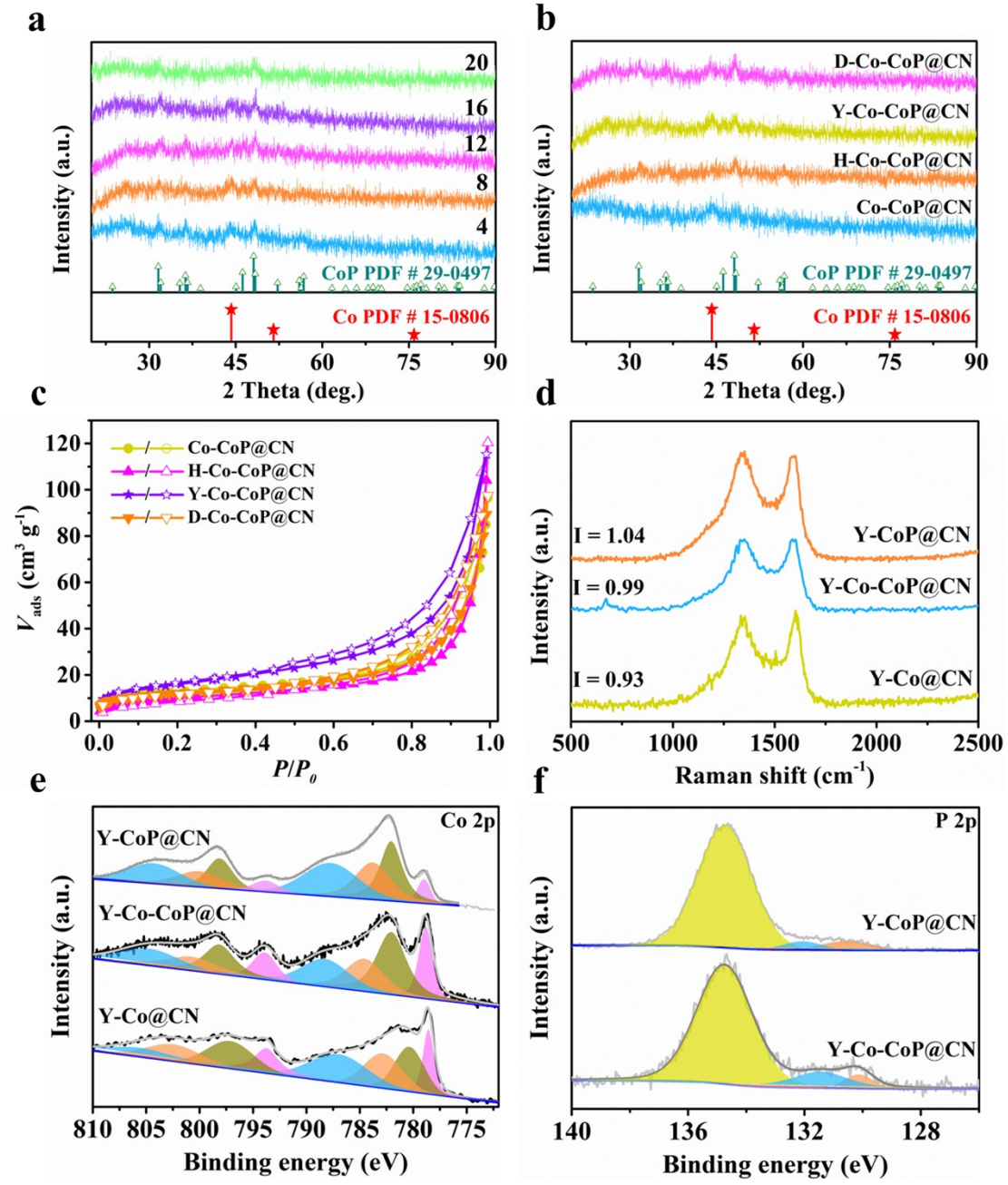

Figure S18. (a) XRD patterns of Y-Co@CN reacted with NaH_2PO_2 at different mass ratios of $m_{NaH2PO2}/m_{Co@CN}$. (b) XRD patterns of Co-CoP@CN, H-Co-CoP@CN, Y-Co-CoP@CN, and D-Co-CoP@CN. (c) N_2 adsorption-desorption isotherms of Co-CoP@CN, H-Co-CoP@CN, Y-Co-CoP@CN, and D-Co-CoP@CN. (d) Raman spectra of Y-Co@CN, Y-Co-CoP@CN, and Y-CoP@CN. (e) Co 2p and (f) P 2p XPS spectra of Y-Co@CN, Y-Co-CoP@CN, and Y-CoP@CN.

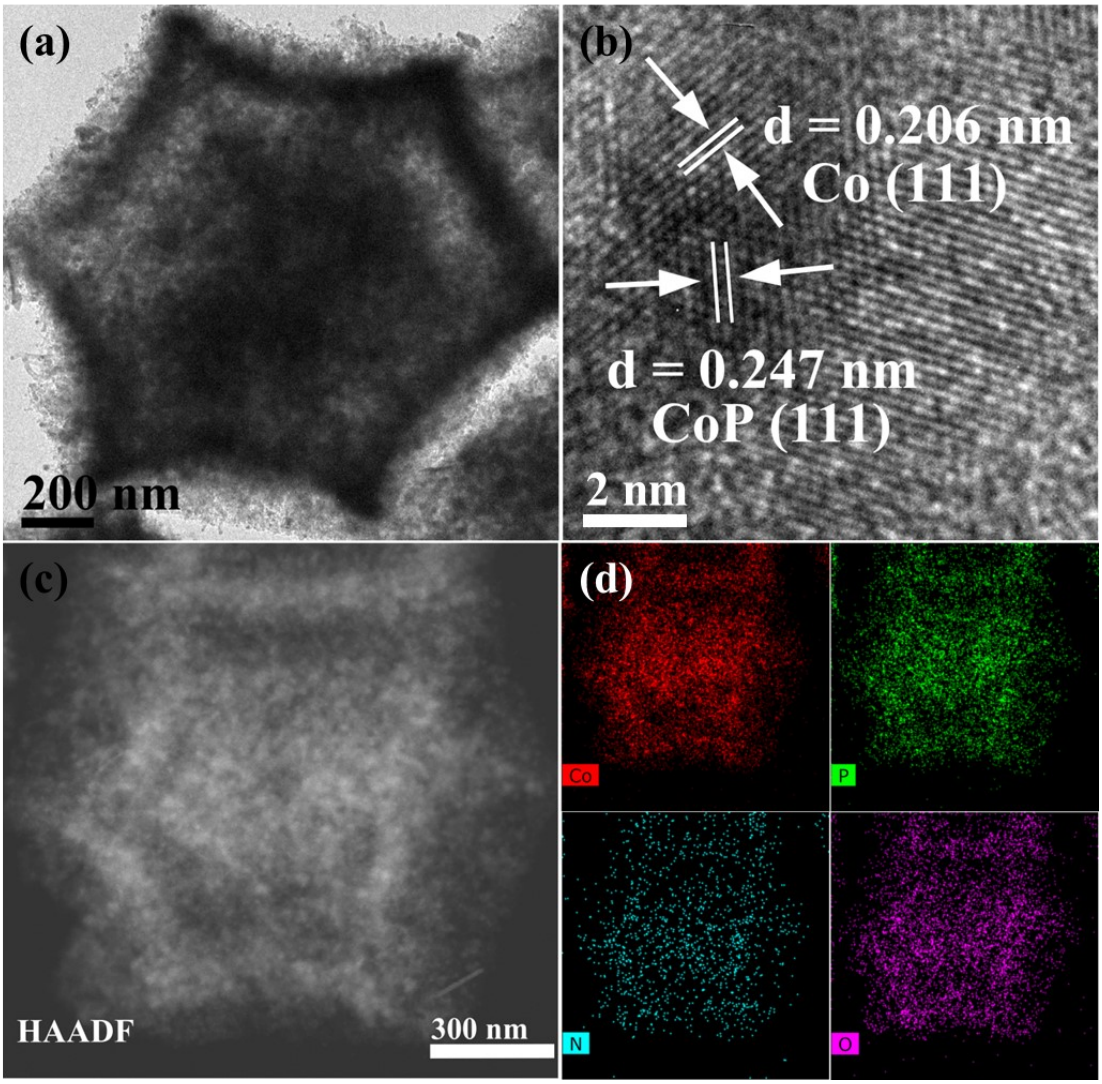

Figure S19. (a) TEM, (b) HRTEM, (c) HAADF-STEM, and (d) EDX mapping images of Y-Co-CoP@CN.

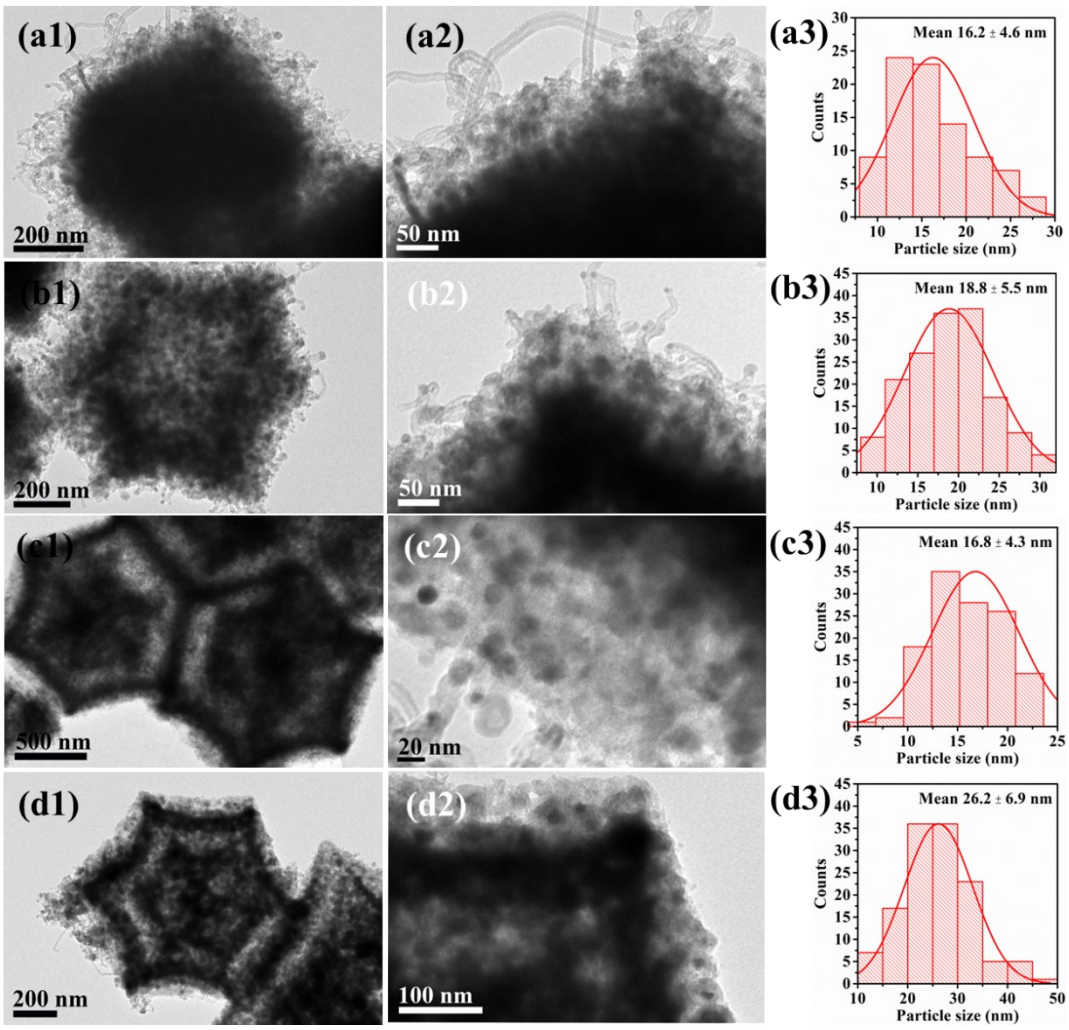

Figure S20. (a1-d1, a2-d2) TEM images, and (a3-d3) the size distributions of Co-CoP NPs. (a1-a3) Co-CoP@CN, (b1-b3) H-Co-CoP@CN, (c1-c3) Y-Co-CoP@CN, and (d1-d3) D-Co-CoP@CN.

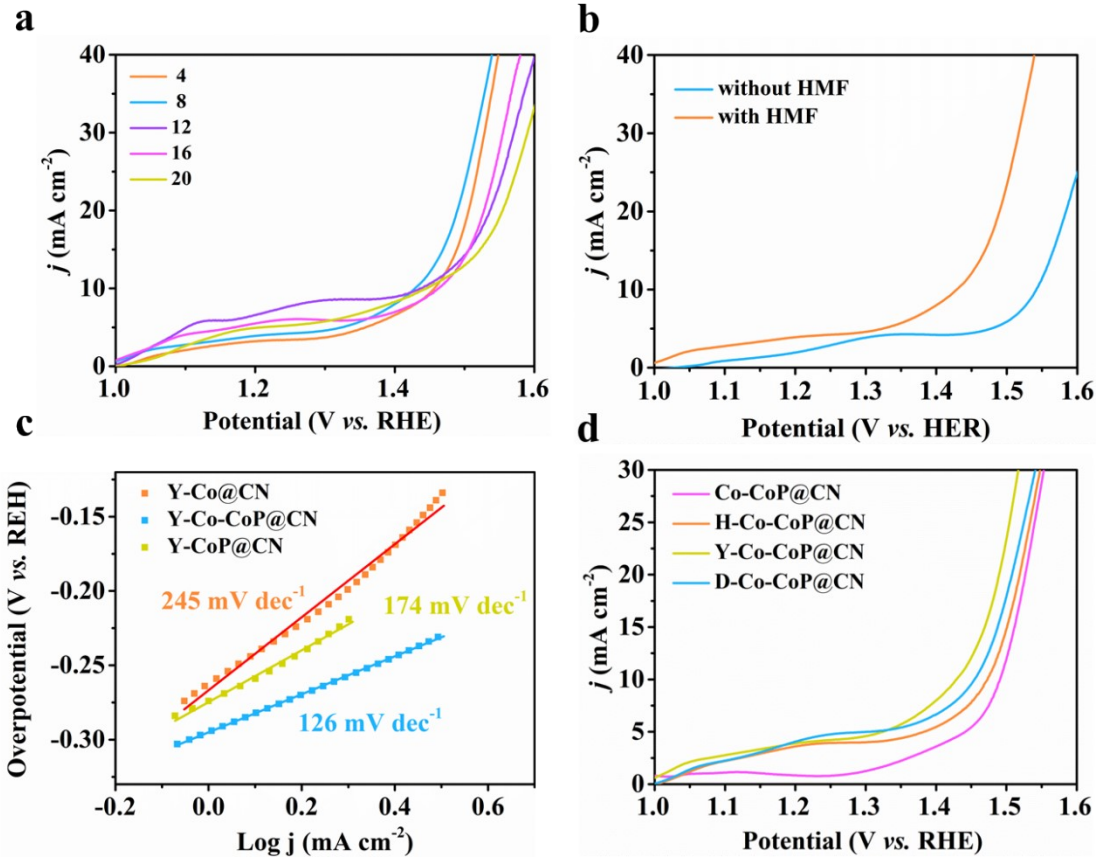

Figure S21. (a) LSV curves of Y-Co@CN reacted with NaH_2PO_2 at different mass ratios of $m_{NaH2PO2}/m_{Co@CN}$ at a scan rate of 5 mV s^{-1} in 0.1 M KOH with 5 mM HMF. (b) LSV curves of Y-Co-CoP@CN in 0.1 M KOH with or without the addition of 5 mM HMF. (c) Tafel slopes of Y-Co@CN, Y-Co-CoP@CN, and Y-CoP@CN. (d) LSV curves of Co-CoP@CN, H-Co-CoP@CN, Y-Co-CoP@CN, and D-Co-CoP@CN at a scan rate of 5 mV s^{-1} in 0.1 M KOH with 5 mM HMF.

As shown in Figure S21d, the electro-catalytic performance of Y-Co-CoP@CN is superior to those of Co-CoP@CN, H-Co-CoP@CN, and D-Co-CoP@CN, further indicating that the construction of yolk-shelled structure is beneficial for providing abundant active sites.

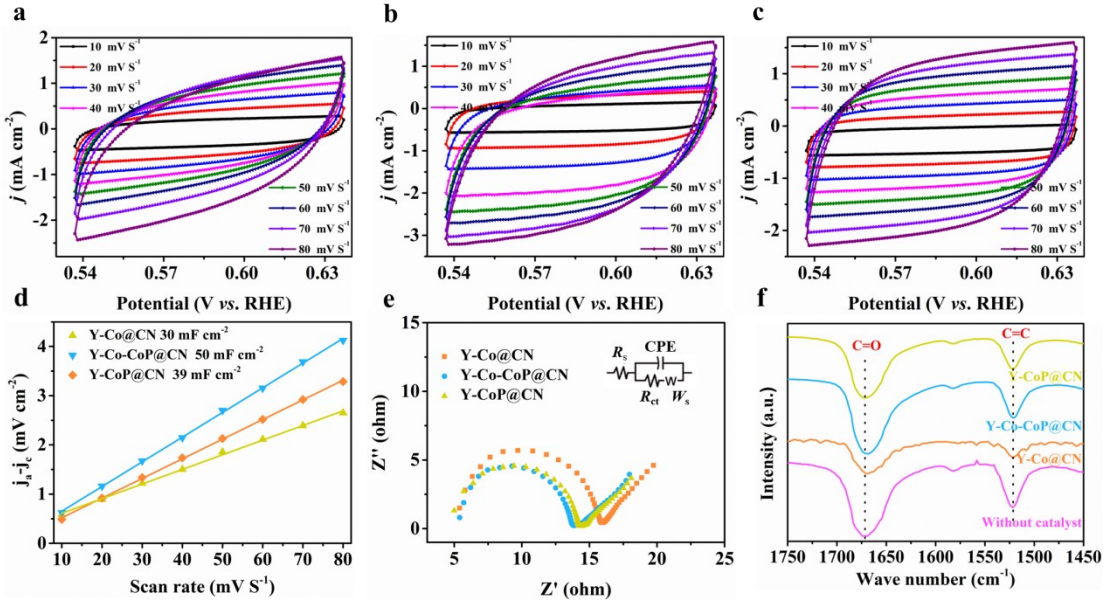

Figure S22. CV curves of (a) Y-Co@CN, (b) Y-Co-CoP@CN, and (c) Y-CoP@CN with 5 mM HMF at different scan rates. (d) Capacitive currents, and (e) Nyquist plots of Y-Co@CN, Y-Co-CoP@CN, and Y-CoP@CN. (f) IR spectra of HMF in the presence of Y-Co@CN, Y-Co-CoS_x@CN, Y-CoS_2@CN or without any catalyst.

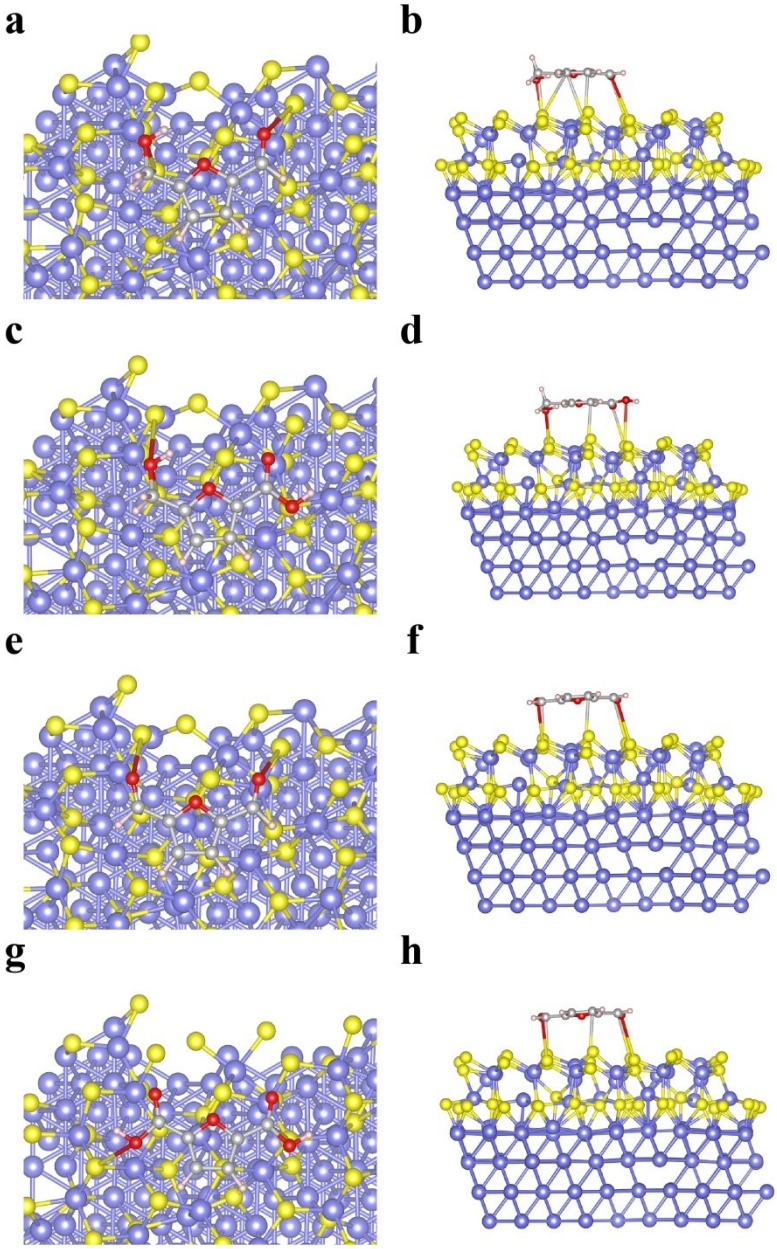

Figure S23. (a, c, e, g) Top, and (b, d, f, h) side views of the configurations for the adsorption of (a, b) HMF, (c, d) HMFCA, (e, f) FFCA, and (g, h) FDCA on Co-CoS_2.

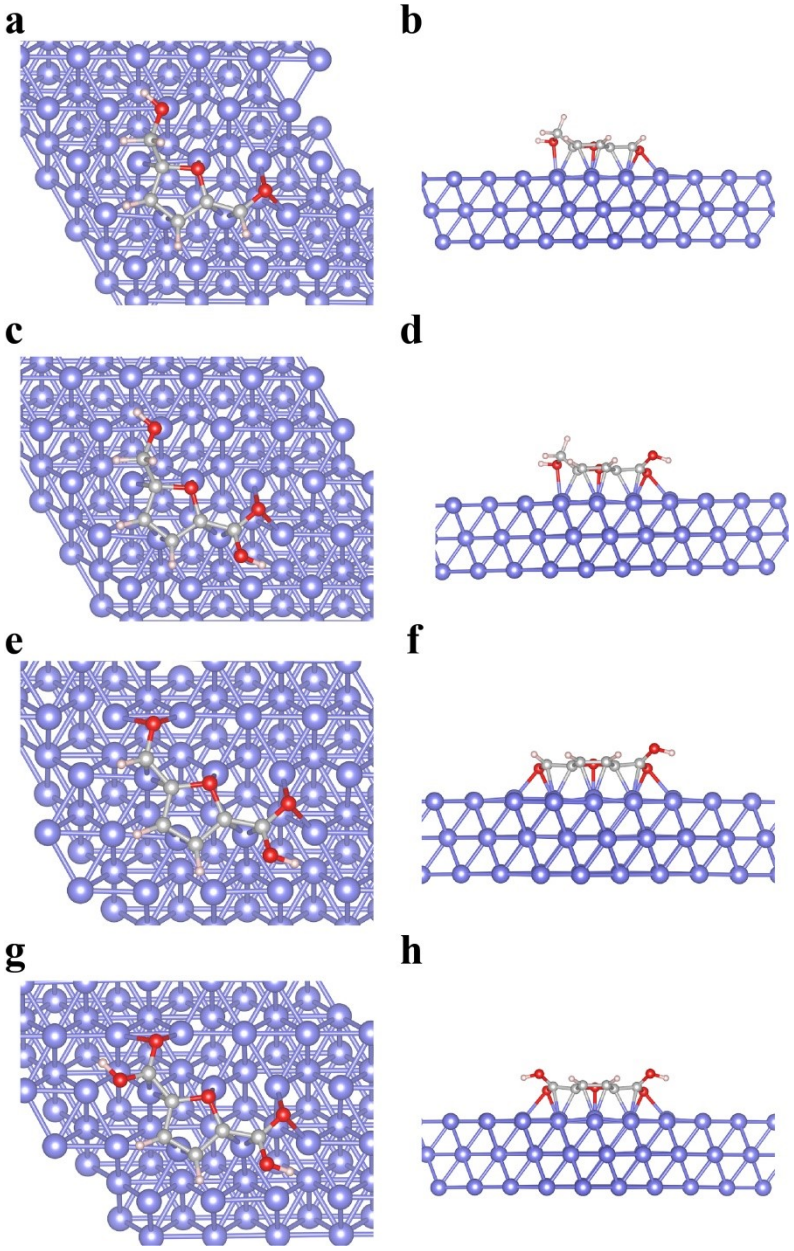

Figure S24. (a, c, e, g) Top, and (b, d, f, h) side views of the configurations for the adsorption of (a, b) HMF, (c, d) HMFCA, (e, f) FFCA, and (g, h) FDCA on Co.

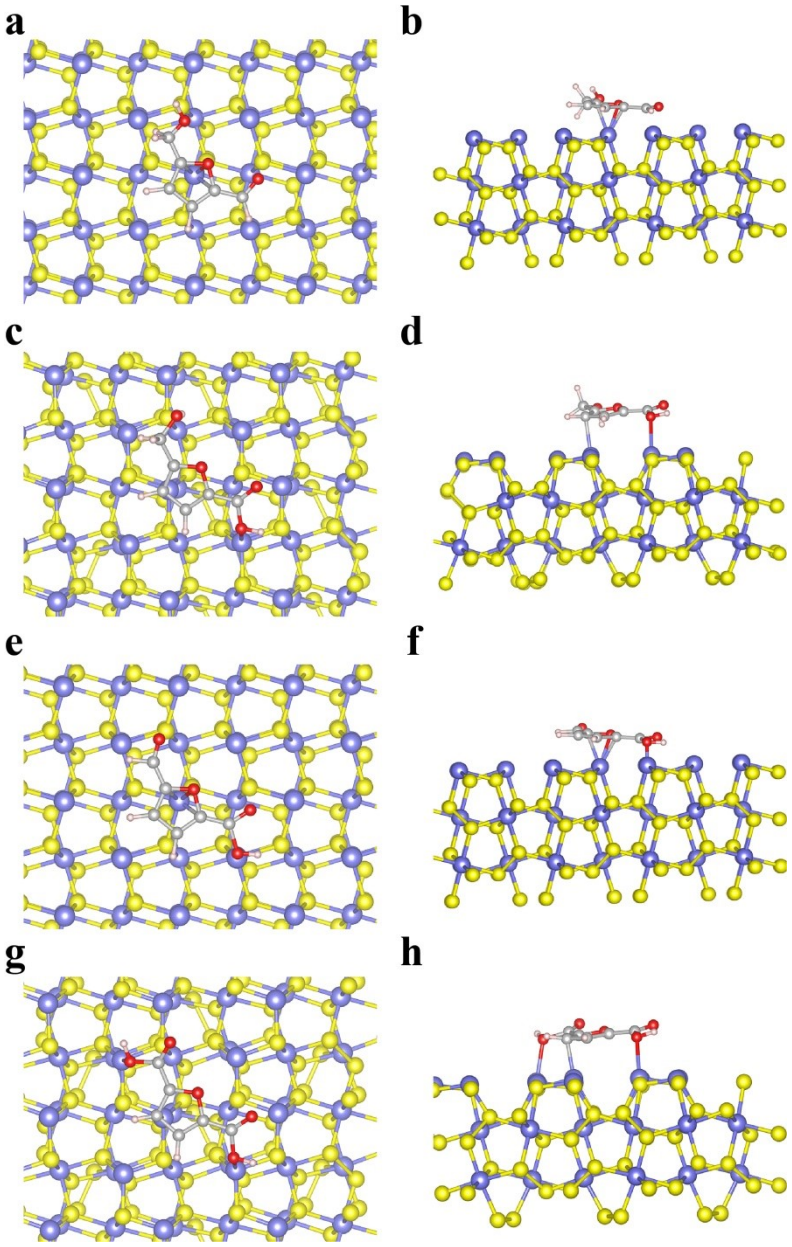

Figure S25. (a, c, e, g) Top, and (b, d, f, h) side views of the configurations for the adsorption of (a, b) HMF, (c, d) HMFCA, (e, f) FFCA, and (g, h) FDCA on CoS_2.

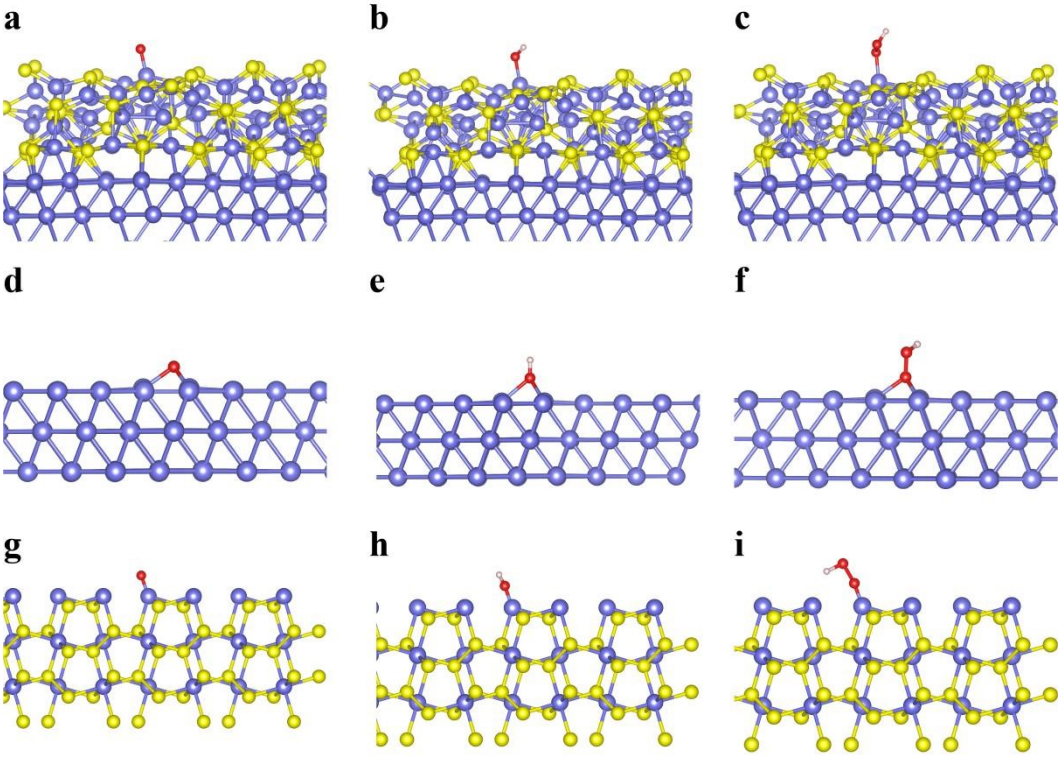

Figure S26. Side views of the configurations of the adsorption of (a, d, g) O, (b, e, h) OH, and (c, f, i) OOH on (a-c) Co-CoS_2, (d-f) Co, and (g-i) CoS_2.

Table S1. Elemental contents of the samples.

Sample	Element content (%)			
	C[a]	N[a]	S[a]	Co[b]
Co-CoS_x@CN	24.4	5.5	13.5	27.0
Co@CN	33.6	3.8	0	32.4
CoS_2@CN	17.5	4.5	22.0	21.3

[a] Determined by elemental analysis.

[b] Determined by AAS.

Table S2. Structural parameters obtained from the global fitting of Co K-edge EXAFS data of Co-Foil, Co@CN, Co-CoS_x@CN, and CoS_2@CN.

Sample	R-factor	Co-S		Co-Co		$\Delta\sigma^2$	δ	ΔE_0 (eV)
		R (Å)	CN	R (Å)	CN	($\times10^{-3}$Å^2)		
Co-foil	0.00058	–	–	2.489±0.002	12	Co: 6±1	0	7.4±0.4
Co@CN	0.025	–	–	2.49±0.01	6.7±1.3	Co: 7±1	0.78	-8.2±2.2
Co-CoS_x@CN	0.0028	2.06±0.03 2.25±0.02	1.8±0.5 4.9±0.7	2.42±0.02	4.5±1.0	S: 7 Co: 12	0.93	-15.8±5.0
CoS_2@CN	0.0094	2.29±0.04	6.2±1.1	2.44±0.02	2.1±0.6	S: 7 Co: 12	1.63	-15.5±4.9

Table S3. Comparison of HMF electrooxidation performances over different catalysts in basic electrolytes.

Catalyst	pH	Oxidation potential (V)	FDCA yield (%)	F.E. (%)	Ref.
Y-Co-CoS_x@CN	**13**	**1.29 (10)**	**96.0**	**93.5**	**This work**
Ni(NS)/CP	13	1.36 (onset)	99.4	95.3	8
$NiCo_2O_4$/NF	13	1.37 (10)	90	100	9
Thick NiOOH	13	1.45 (onset)	96.0	96.0	10
NiCoBDC-NF	13	1.55 (10)	99	78.8	11
copper oxide	13	1.58 (onset)	96.4	95.3	12
CuxS@NiCo-LDH	14	1.19/(onset)	99	99	13
CoO–$CoSe_2$	14	1.3 (onset)	99.0	97.9	14
Co_3O_4 NW/NF	14	1.31 (10)	96.8	96.6	15
hp-Ni	14	1.35 (onset)	98	98	16
VN/NF	14	1.36 (10)	96	84	17
CoB/NF	14	1.39 (onset)	94	98	18
Co−P/CF	14	1.38 (20)	90	-	19
Ir/Co_3O_4	14	1.38 (10)	98	98	20
$CuCo_2O_4$/NF	14	1.40 (10)	93.7	94	21
$NiCo_2O_4$/NF	14	1.47 (10)	90.8	87.5	21
Ni_3S_2/NF	14	1.47 (10)	98	98	22
MoO_2-FeP@C	14	1.49 (10)	98.6	97.8	23

$Pt/Ni(OH)_2$	14	1.50 (37)	100	98.7	24
NiCoFe-LDHs	14	1.52 (10)	95.5	84.9	25

Table S4. The component of atomic orbital of Co and C in Co-C molecular orbitals.

	Co-CoS_2	Co	CoS_2
Co($3d_{xy}$)-C(2p)	21.01	11.76	3.03
Co($3d_{yz}$)-C(2p)	4.84	33.22	45.35
Co($3d_{x2-y2}$)-C(2p)	12.37	12.33	10.58
Co($3d_{xz}$)-C(2p)	30.31	14.16	1.54
Co($3d_{z2}$)-C(2p)	31.47	39.11	39.49

References

[1] P. Giannozzi, S. Baroni, N. Bonini, M. Calandra, R. Car, C. Cavazzoni, D. Ceresoli, G. L. Chiarotti, M. Cococcioni, I. Dabo, A. Dal Corso, S. Fabris, G. Fratesi, S. de Gironcoli, R. Gebauer, U. Gerstmann, C. Gougoussis, A. Kokalj, M. Lazzeri, L. Martin-Samos, N. Marzari, F. Mauri, R. Mazzarello, S. Paolini, A. Pasquarello, L. Paulatto, C. Sbraccia, S. Scandolo, G. Sclauzero, A. P. Seitsonen, A. Smogunov, P. Umari and R. M. Wentzcovitch, *J. Phys.: Condens. Matter,* 2009, **21**, 395502.

[2] P. Giannozzi, O. Andreussi, T. Brumme, O. Bunau, M. Buongiorno Nardelli, M. Calandra, R. Car, C. Cavazzoni, D. Ceresoli, M. Cococcioni, N. Colonna, I. Carnimeo, A. Dal Corso, S. de Gironcoli, P. Delugas, R. A. DiStasio Jr, A. Ferretti, A. Floris, G. Fratesi, G. Fugallo, R. Gebauer, U. Gerstmann, F. Giustino, T. Gorni, J. Jia, M. Kawamura, H. Y. Ko, A. Kokalj, E. Küçükbenli, M. Lazzeri, M. Marsili, N. Marzari, F. Mauri, N. L. Nguyen, H. V. Nguyen, A. Otero-de-la-Roza, L. Paulatto, S. Poncé, D. Rocca, R. Sabatini, B. Santra, M. Schlipf, A. P. Seitsonen, A. Smogunov, I. Timrov, T. Thonhauser, P. Umari, N. Vast, X. Wu and S. Baroni, *J. Phys.: Condens. Matter,* 2017, **29**, 465901.

[3] J. P. Perdew; K. Burke and M. Ernzerhof, *Phys. Rev. Lett.,* 1996, **77**, 3865.

[4] P. E. Blöchl, O. Jepsen and O. K. Andersen, *Phys. Rev. B,* 1994, **49**, 16223.

[5] G. Kresse and D. Joubert, *Phys. Rev. B,* 1999, **59**, 1758.

[6] H. J. Monkhorst and J. D. Pack. *Phys. Rev. B,* 1976, **13**, 5188.

[7] R. Dronskowski and P. E. Blöchl, *J. Phys. Chem.,* 1993, **97**, 8617-8624.

[8] X. Lu, K. H. Wu, B. Zhang, J. Chen, F. Li, B. J. Su, P. Yan, J. M. Chen and W. Qi, *Angew. Chem. Int. Ed.,* 2021, **60**, 14528.

[9] L. Gao, Y. Bao, S. Gan, Z. Sun, Z. Song, D. Han, F. Li and L. Niu, *ChemSusChem*, 2018, **11**, 2547.

[10] B. J. Taitt, D. H. Nam, K. S. Choi, B. J. Taitt, D. H. Nam and K. S. Choi, *ACS Catal*., 2019, **9**, 660.

[11] M. Cai, Y. Zhang, Y. Zhao, Q. Liu, Y. Li and G. Li, *J. Mater. Chem. A,* 2020, **8**, 20386.

[12] D. H. Nam, B. J. Taitt and K. S. Choi, *ACS Catal.,* 2018, **8**, 1197.

[13] X. Deng, X. Kang, M. Li, K. Xiang, C. Wang, Z. Guo, J. Zhang, X. Z. Fu and J. L. Luo. *J. Mater. Chem. A,* 2020, **8**, 1138.

[14] X. Huang, J. Song, M. Hua, Z. Xie, S. Liu, T. Wu, G. Yang and B. Han. *Green Chem.,* 2020, **22**, 843.

[15] Z. Zhou, C. Chen, M. Gao, B. Xia and J. Zhang, *Green Chem.,* 2019, **21**, 6699.

[16] B. You, X. Liu, X. Liu and Y. Sun. *ACS Catal.,* 2017, **7**, 4564.

[17] S. Li, X. Sun, Z. Yao, X. Zhong, Y. Cao, Y. Liang, Z. Wei, S. Deng, G. Zhuang, X. Li and J. Wang, *Adv. Funct. Mater.,* 2019, **29**, 1904780.

[18] Weidner J, Barwe S, Sliozberg K, S. Piontek, J. Masa, U.-P. Apfel and W. Schuhmann, Beilstein J. Org. Chem., 2018, **14**, 1436-1445.

[19] N. Jiang, B. You, R. Boonstra, I. M. Terrero Rodriguez and Y. Sun, *ACS Energy Lett.*, 2016, **1**, 386.

[20] Y. Lu, T. Liu, C. L. Dong, Y. C. Huang, Y. Li, J. Chen, Y. Zou and S. Wang, *Adv. Mater.,* 2021, **33**, 2007056.

[21] Y. Lu, C. L. Dong, Y. C. Huang, Y. Zou, Z. Liu, Y. Liu, Y. Li, N. He, J. Shi and S. Wang, *Angew. Chem., Int. Ed.,* 2020, **59**, 19215.

[22] B. You, X. Liu, N. Jiang and Y. Sun, *J. Am. Chem. Soc.,* 2016, **138**, 13639.

[23] G. Yang, Y. Jiao, H. Yan, Y. Xie, A. Wu, X. Dong, D. Guo, C. Tian, and H. Fu,

Adv. Mater., 2020, **32**, 2000455.

[24] B. Zhou, Y. Li, Y. Zou, W. Chen, W. Zhou, M. Song, Y. Wu, Y. Lu, J. Liu, Y. Wang and S. Wang, *Angew. Chem. Int. Ed.,* 2021, **60**, 22908.

[25] M. Zhang, Y. Liu, B. Liu, Z. Chen, H. Xu and K. Yan, *ACS Catal.,* 2020, **10**, 5179.